Research Article

Comprehensive Numerical Investigations of Unsteady Internal Flows and Cavitation Characteristics in Double-Suction Centrifugal Pump

Xuelin Tang,[1,2] **Mingde Zou,**[1] **Fujun Wang,**[1,2] **Xiaoqin Li,**[1,2] **and Xiaoyan Shi**[1,2]

[1]*College of Water Resources and Civil Engineering, China Agricultural University, Beijing 100083, China*
[2]*Beijing Engineering Research Center of Safety and Energy Saving Technology for Water Supply Network System,
 China Agricultural University, Beijing 100083, China*

Correspondence should be addressed to Xuelin Tang; xl-tang@mail.tsinghua.edu.cn

The RNG k-ε turbulence model combined with cavitation model was used to simulate unsteady cavitating flows inside a double-suction centrifugal pump under different flow rate conditions based on hexahedral structured grid. The numerical external characteristic performances agree well with the experimental performances. The predicted results show that the turbulence kinetic energy and the turbulence dissipation rate inside the impeller at design flow rate are lower than those at other off-design flow rates, which are caused by various vortexes. Based on frequency-domain analyses in the volute casing, the blade passing frequency is the dominant one of the pressure fluctuations except the vicinity of volute tongue for all operating cases, and the dominant frequency near the volute tongue ranges from 0 to 0.5 times the blade passing frequency for other off-design points, while the blade passing one near the volute tongue is the dominant one of the pressure fluctuations at design point. The increase of flow rate reduces the pressure fluctuations amplitude. For cavitation cases, the blade loading of the middle streamline increases a bit during the initial stage, but, for serious cavitation, the blade loading near the blade inlet reduces to 0 and even negative values, and the serious cavitation bubbles block the blade channels, which results in a sharp drop in pump head. Under noncavitation condition, the predicted power related to the pressure in the impeller channels increases from the inlet to the exit, while, under different cavitation conditions at the design flow rate, these power-transformation distributions in the impeller channels show that these power conversions are affected by the available NPSH$_a$ and the corresponding work in leading regions of the blades increases increases gradually a bit, and then it increases sharply in the middle regions, but it decreases in the blade trailing regions and is greatly influenced by secondary flows.

1. Introduction

Centrifugal pumps are the most commonly used type among various pumps, where double-suction centrifugal pumps have advantages of large flow rate, high efficiency, high head, and so forth, which occupies a large proportion of the pump products. The internal flow inside a double-suction centrifugal pump is unsteady and extremely complex. There are some possible phenomena in the flow, such as rotor-stator interaction, rotating stalling, and cavitation [1–3]. With rapid development in computer technology and computational fluid dynamics (CFD), the CFD method is a good tool to investigate complex turbulent flows inside pumps [4]. In

numerical simulation of a centrifugal pump, blade angles, blade number, and turbulence model have great effect on the predicted performances of centrifugal pump [5]. Shigemitsu et al. [6] numerically studied three types of impellers with different outlet angles in the mini turbo-pumps and found that the change of the blade outlet angle has effect on performance and internal flows in mini turbo-pumps. Chakraborty et al. [7] analyzed the static pressure distribution and characteristics of the two-dimensional (2D) incompressible flow inside a centrifugal pump's impellers with different blade numbers, and the predicted results displayed that the head and static pressures of the pump increase with the increase of the blade number, while the efficiency with seven-blade

pump is optimal. González et al. [8] investigated numerically the internal flow inside a double-suction centrifugal machine in the pump operation mode and found that the flow in the double-suction chamber is uniform at design flow rate but has a strong unsteady characteristic at off-design flow rates. At the same time, the cavitation is a common phenomenon in centrifugal pumps. When the pressure inside the pump is below the saturation water vapor pressure, cavitation may occur. It will cause noise, performance breakdown, and costly damage to hydraulic machineries [9]. Liu et al. [10] used the standard RNG k-ε model and two modified RNG k-ε models, that is, density correction based model (DCM) and filter-based model (FBM), to simulate the unsteady attached sheet-cavitating flows in centrifugal pumps, and the studies suggested that all the turbulence models rarely affect the evolution of cavitation bubbles, but the advanced turbulence model can significantly improve the prediction precision of head coefficients and critical cavitation numbers. Thai and Lee [11] predicted the cavitation characteristics of the centrifugal pump with two types of short and long blades at on-design and off-design points, respectively. The numerical results showed that the pump can safely operate without cavitation at design point, but the cavitation develops inhomogeneously in the blade channels at off-design points.

The main focus of our work is to investigate the hydraulic performance and the cavitation performance of a double-suction centrifugal pump. Firstly, based on ANSYS CFX solver, the RNG k-ε turbulence model was used to calculate the unsteady flow fields inside the pump without cavitation at different flow rates. The predicted external characteristics of the pump were in good agreement with the experimental ones. For different NPSH$_a$, the blade loading and the vapor volume fraction for cavitation flows in the impeller were simulated numerically and analyzed systematically at design point, and the studies on the influence of the cavitation and secondary flows on power distributions were carried out.

2. Basic Parameters and Computational Grids

The flow characteristics inside a double-suction centrifugal pump with a specific speed n_s of 160 (r/min·(m³/s)$^{1/2}$·m$^{-3/4}$) was investigated here, and the main hydraulic components of the pump include a suction chamber, an impeller, and volute casing. The basic geometric parameters of this pump are the pump inlet diameter D_{in} of 300 mm, the pump outlet diameter D_{out} of 250 mm, the 355 mm cutwater diameter D_3 of the volute, the impeller inlet diameter D_1 of 200 mm, and the impeller outlet diameter D_2 of 348 mm. The blades on the two sides of the impeller are arranged in a staggered angle of 30 degrees shown in Figure 1, and the blade number N on each side is 6. In addition, the rated rotating speed n is 1480 r/min and the design flow rate Q_d is 808.38 m³/h. The experimental performance parameters are listed in Table 1, where Q, H, P, and η represent the flow rate, the pump head, the shaft power, and the pump efficiency, respectively.

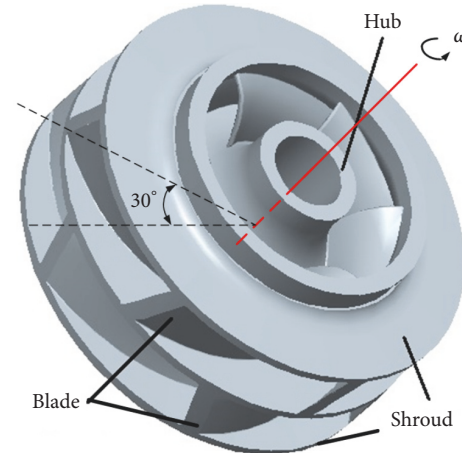Based on 3D CAD software, the computational domain of the pump was constructed as shown in Figure 2. The
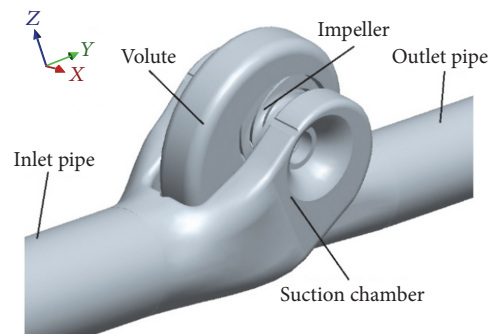

Figure 1: Pump impeller.

Figure 2: Computational domain.

Cartesian x, y, and z coordinate system is adopted here; the x axis is the rotating one of the impeller and $x = 0$ m for the y-z symmetry plane of the suction chamber. The computational grids based on the hexahedral structured grid were generated as shown in Figure 3, and the grid quality value calculated based on determinant $3 \times 3 \times 3$ method is above 0.4. A localized refinement of grids was employed near the volute tongue and the blade leading and trailing edges of the impeller to capture accurately the flow field structure. Also, 4 different grid systems were used to perform the independent-grid verification at design flow rate as shown in Figure 4. It can be seen that when the grid number is more than 2.39×10^6, the predicted head will not change apparently and its increase rates are less than 0.2%. So the final grid number for the computation was selected as 2.39×10^6, and the node and grid numbers of each hydraulic component are listed in Table 2. This computation was done on a PC (configuration: Intel (R) Core (TM) 2 Quad CPUs; memory, 8 G).

3. Turbulence and Cavitation Models

3.1. Turbulence Model. The RNG k-ε turbulence model proposed by Yakhot and Orszag [12] has its unique advantages
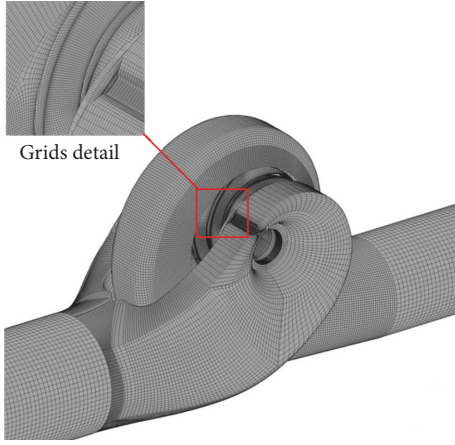
Figure 3: Computational grids.

Table 2: The node and grid numbers of each of the hydraulic components.

Hydraulic components	Suction chamber	Impeller	Volute casing
Node number ($\times 10^6$)	1.01	0.99	0.59
Grid number ($\times 10^6$)	0.96	0.87	0.56

paper. The RNG k-ε turbulence model is as follows:

$$
\begin{aligned}
\frac{\partial (\rho k)}{\partial t} + \frac{\partial (\rho k u_i)}{\partial x_i} &= \frac{\partial}{\partial x_j} \left[\alpha_k (\mu + \mu_t) \frac{\partial k}{\partial x_j} \right] + G_k \\
&\quad + \rho \varepsilon, \\
\frac{\partial (\rho \varepsilon)}{\partial t} + \frac{\partial (\rho \varepsilon u_i)}{\partial x_i} &= \frac{\partial}{\partial x_j} \left[\alpha_\varepsilon (\mu + \mu_t) \frac{\partial \varepsilon}{\partial x_j} \right] + C_{1\varepsilon}^* \frac{\varepsilon}{k} G_k \\
&\quad - C_{2\varepsilon} \rho \frac{\varepsilon^2}{k}, \\
\mu_t &= \rho C_\mu \frac{k^2}{\varepsilon}, \\
G_k &= \mu_t \left(\frac{\partial u_i}{\partial x_j} + \frac{\partial u_j}{\partial x_i} \right) \frac{\partial u_i}{\partial x_j}, \\
C_{1\varepsilon}^* &= C_{1\varepsilon} - \frac{\eta (1 - \eta/\eta_0)}{1 + \beta \eta^3}, \\
\eta &= \frac{\sqrt{2}}{2} \left(\frac{\partial u_i}{\partial x_j} + \frac{\partial u_j}{\partial x_i} \right) \frac{k}{\varepsilon},
\end{aligned}
\tag{1}
$$

where μ_t stands for the turbulent viscosity and G_k represents the turbulence production due to turbulent forces. The model coefficients are taken as $C_{1\varepsilon} = 1.42$, $C_{2\varepsilon} = 1.68$, $C_\mu = 0.0845$, $\alpha_k = \alpha_\varepsilon = 1.39$, $\eta_0 = 4.377$, and $\beta = 0.012$.
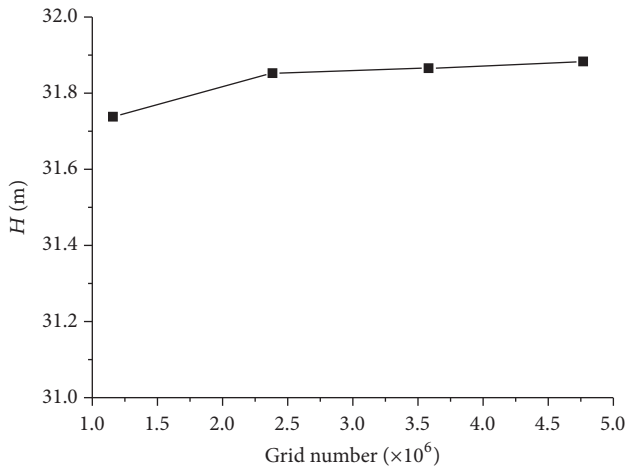

Figure 4: Head variation with grid number of pump grid system at design flow rate.

Table 1: The experimental performance parameters of pump at different flow rates.

Flow rates	Q (m^3/h)	n (r/min)	H (m)	P (kW)	η (%)
$0.57Q_d$	459.48	1480	39.17	63.792	76.84
$0.72Q_d$	583.38	1480	37.22	69.411	85.2
$0.82Q_d$	659	1480	35.57	73.276	87.11
$0.91Q_d$	738.74	1480	33.44	76.16	88.33
$1.00Q_d$	808.38	1480	31.5	77.757	89.18
$1.07Q_d$	861.4	1480	29.65	79.772	87.18
$1.16Q_d$	936.4	1480	26.71	82.157	82.91
$1.20Q_d$	971.7	1480	24.55	81.495	79.73

of turbulent viscosity modified based on standard k-ε turbulence model and allowing high curvature and strain rate for the rotation and the swirl flow of the average flow. So the turbulence model was adopted to investigate the complex turbulence flows in double-suction centrifugal pump in this

3.2. Cavitation Model. It is necessary to introduce a two-phase mixture model and a cavitation model in cavitating flow calculation. The basic governing equations of the two-phase mixture are based on the Navier-Stokes equations [13], and the continuity equation of the two-phase mixture is given as

$$
\frac{\partial \rho_m}{\partial t} + \nabla \cdot (\rho_m \mathbf{u}) = 0;
\tag{2}
$$

the momentum equation is as follows:

$$
\begin{aligned}
\frac{\partial (\rho_m \mathbf{u})}{\partial t} + \nabla \cdot (\rho_m \mathbf{u}) &= -\nabla p + \frac{1}{3} \nabla \left[(\mu_m + \mu_t) \nabla \cdot \mathbf{u} \right] \\
&\quad + \nabla \left[(\mu_m + \mu_t) \nabla \cdot \mathbf{u} \right].
\end{aligned}
\tag{3}
$$

The cavitation model used is the transport equation deduced from the Rayleigh-Plesset equation [14]. Considering the growth and collapse of cavitation bubbles, the mass transport equation is expressed as

$$\frac{\partial\left(\alpha_{v}\rho_{v}\right)}{\partial t} + \nabla \cdot \left(\alpha_{v}\rho_{v}\mathbf{u}\right) = m_{\mathrm{eva}} - m_{\mathrm{con}},$$

$$m_{\mathrm{eva}} = C_{\mathrm{eva}}\frac{3\alpha_{v}\rho_{v}}{R_{b}}\sqrt{\frac{2}{3}\frac{\max\left(p_{v} - p, 0\right)}{\rho_{l}}}, \tag{4}$$

$$m_{\mathrm{con}} = C_{\mathrm{con}}\frac{3\alpha_{v}\rho_{v}}{R_{b}}\sqrt{\frac{2}{3}\frac{\max\left(p - p_{v}, 0\right)}{\rho_{l}}},$$

where ρ_{m} represents the mass density of the two-phase mixture; $\mathbf{u}$ represents the velocity vector of the two-phase mixture; μ_{m} represents the dynamic viscosity coefficient of the two-phase mixture; α_{v} represents the volume fraction of bubbles; ρ_{v} and ρ_{l} represent the mass densities of vapor and liquid, respectively; m_{eva} and m_{con} represent the evaporation rate and condensation rate of water vapor in unit volume, respectively; C_{eva} and C_{con} represent the evaporation rate coefficient and condensation rate coefficient of water vapor in unit volume, respectively; the saturated vapor pressure p_{v} of water is 3170 Pa at the temperature of 25°C, and the average diameter of the bubbles R_{b} is 2×10^{-6} m.

4. Numerical Methods and Boundary Conditions

The ANSYS CFX solver was selected in this study. In the discrete process of governing equations, the time-dependent terms were discretized with the second-order backward Euler scheme, the second-order central scheme was used for the diffusive terms, and the high resolution was used to solve the convection terms. In the ANSYS CFX solver, the high resolution is a special discrete scheme for the convection terms. When dealing with the convection terms, the convective fluxes at the integral points are approximated by those of the adjacent nodes, which can be expressed as

$$\varphi_{p} = \varphi_{n} + \beta\nabla\varphi \cdot \Delta\overrightarrow{r}, \tag{5}$$

where φ_{p} and φ_{n} denote the convective fluxes at the integral points and the upwind nodes, respectively; $\nabla\varphi$ denotes the convective flux gradients within the control volumes; β represents the coefficient of the numerical convection correction; $\Delta\overrightarrow{r}$ is the vector from the upwind node to the integral point. Different discrete schemes differ in choices for β and $\nabla\varphi$. In the high resolution scheme, β at each node is computed to be as close to 1 (not exceed 1) as possible by using a special nonlinear recipe that is based on the boundedness principles used by Barth and Jespersen [15]. Obviously, (5) indicates that the high resolution scheme preferentially uses the second-order backward Euler scheme and reverts to the first-order backward Euler scheme only when the convective flux gradients are very small somewhere within the control volumes.

The solving process was based on the fully implicit grid coupling solution technique. The rotating period T of the impeller was 0.0405 s. The time step was set to 2.252×10^{-4} s in the transient calculation. Number of periods per time step was set to 10 to achieve the periodic unsteady solution convergence, and the convergence criterion was set to RMS residuals of 10^{-5}. The steady solution was used to initialize the unsteady calculation.

In order to minimize edge effects and to improve numerical stability, two extension domains were added upstream and downstream. The normal velocity condition was used at the inlet. The static pressure condition was used at the outlet and the pressure values were given by the experimental data. The dynamic-static coupling between the suction chamber and the impeller was realized by setting the rotor frozen interface and the same setting was also used for the dynamic-static coupling between the impeller and the volute casing. Simultaneously, the no-slip boundary condition was used on the solid wall, and the near-wall region was treated by using scalable wall function. The cavitating flow was simulated by gradually reducing the static pressure at the outlet, and the reference pressure value of fluid domain was set to 0. Besides, the cavitating flow calculation was initialized by the solution of single-phase noncavitating flow calculation. At the beginning of cavitating flow calculation, the volume fraction of vapor phase was set to 0, and that of liquid phase was set to 1.

5. Analyses of Internal Flow in Noncavitation Condition

5.1. The External Characteristics Curves. The numerical efficiency is only the hydraulic efficiency η_{h}. In fact, there are also mechanical loss and volumetric loss in the pump operation. In order to do comparisons between the numerical results and the experimental data, the total pump efficiency η must be considered, which is actually composed of the hydraulic efficiency η_{h}, the mechanical efficiency η_{m}, and the volumetric efficiency η_{v} [16], expressed as

$$\eta = \eta_{h}\eta_{m}\eta_{v}. \tag{6}$$

The mechanical efficiency η_{m} is calculated by the empirical formula as follows:

$$\eta_{m} \approx 1 - 0.07\frac{1}{\left(n_{s}/100\right)^{7/6}}. \tag{7}$$

The volumetric efficiency η_{v} caused by volumetric loss is calculated by the following empirical formula:

$$\eta_{v} \approx \frac{1}{1 + 0.68n_{s}^{-2/3}}. \tag{8}$$

It can be seen from Figure 5 that, with the increase of flow rate, the pump head drops gradually, while the pump shaft power rises. The calculated pump head is larger than the experimental data at large flow rates but smaller than the experimental data at small flow rates. The trends between the
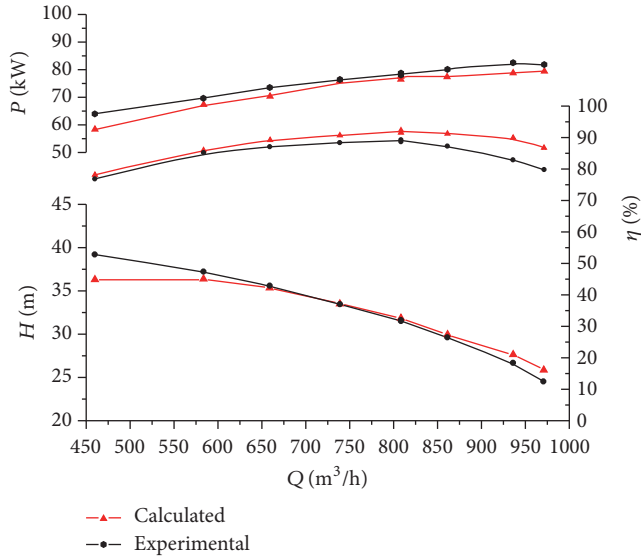
FIGURE 5: Comparison between performance curves.

calculated pump shaft power and the experimental data are roughly identical, and the calculated value is lower than the experimental one. The efficiency increases with the increase of flow rate at first, and it reaches the highest point at design flow rate; then as the flow rate continues to increase, it begins to decline gradually. The calculated efficiency is higher a little than the experimental one. Overall, the calculated results agree well with the experimental data.

5.2. Static Pressure Distribution in the Impeller. Viewed from the pump inlet, the pump is divided by the *y-z* symmetry plane of the suction chamber into two parts, that is, left part and right one. Figure 6 shows the static pressure distributions on the hubs of the right part and the left one at different flow rates. It can be seen that the static pressure increases gradually from the impeller inlet to the outlet, and the fluid flows inside the left and right parts are symmetric. An obvious low-pressure region appears near the impeller inlet and near the blade suction surface; the static pressure reaches the lowest and cavitation may happen here as shown in Figure 7. When the fluid enters into the impeller channel, it can get the energy due to the work done by the impeller. It is shown in Figure 7 that the static pressure on pressure surface is higher than that on suction surface, and the pressure difference causes the moment of resistance on rotating impeller.

5.3. Analysis of Pressure Fluctuations in the Volute Casing. There is dynamic-static coupling between the volute casing and the impeller, which may cause the pressure fluctuations and affects the stability of the pump. The pressure fluctuations characteristics are usually characterized by pressure coefficient C_p [17], which is defined as

$$C_p = \frac{p - \overline{p}}{0.5\rho u_2^2}, \tag{9}$$

where p represents the transient pressure, $\overline{p}$ is the average value of all the transient pressure at all monitoring points for

8 rotor revolutions, u_2 represents the circumferential velocity at the impeller outlet, and ρ is the fluid mass density.

In order to monitor the pressure fluctuations in the volute casing, 6 monitoring points (namely, $V0, V1, V2, V3, V4, V5$) are set on the symmetric plane of the volute casing, as illustrated in Figure 8. The sampling frequency f_s is 4440 Hz ($f_s = 1/T$) and the results for $8T$ sampling time are selected for analysis. The blade passing frequency f_b is 296 Hz.

At design flow rate, the dominant frequency of the pressure fluctuations at monitoring point $V0$ is mainly caused by the blade passing frequency shown in Figure 9, followed by the frequencies that are 0~0.5 times the blade passing frequency. However, at monitoring points from $V1$ to $V5$, the blade passing frequency is the dominant frequency of the pressure fluctuations, followed by the second harmonic of the blade passing frequency. At off-design flow rates, the dominant frequency of the pressure fluctuations at monitoring point $V0$ is 0~0.5 times the blade passing frequency, and, in contrast, the dominant frequency of the pressure fluctuations at monitoring points from $V1$ to $V5$ is mainly brought about by the blade passing frequency, followed by the frequencies that are 0~0.5 times the blade passing frequency. Besides, the pressure fluctuations amplitudes at all monitoring points in volute casing decrease gradually with the increase of the flow rate.

5.4. Distributions of the Relative Velocity and Streamline in the Hydraulic Components. Figure 10 shows the relative velocity and streamline distributions in the impeller and the volute casing at different flow rates. At the flow rate of $0.72Q_d$, the relative velocity distribution in the impeller is nonaxisymmetric; there is an obvious low-velocity region in the impeller channel near the volute tongue and an axial vortex appears in the low-velocity region. In most regions of the impeller channels, the relative velocity is higher near the suction surface than that near pressure surface of the blade. The relative velocity and the streamlines in the volute casing distribute nonsmoothly. At the flow rate of $1.0Q_d$, the relative velocity distribution in the impeller appears axisymmetric and uniform, and the axial vortex in blade channel disappears at flow rate of $0.72Q_d$. What is more, the relative velocity and the streamlines in the volute casing distribute much more smoothly. The relative velocity and streamline distributions in the impeller and volute casing at the flow rate of $1.2Q_d$ are roughly similar to those at the flow rate of $1.0Q_d$, but the flow in the impeller at the flow rate of $1.2Q_d$ is less axisymmetric than that at flow rate of $1.0Q_d$. In addition, it can be concluded from Figure 10 that, under the off-design conditions, a low-velocity region will appear in the vicinity of volute outlet, which is caused by the reverse flow.

Relative velocity and streamline distributions on the plane of $x = 0.16$ m in the suction chamber are shown in Figure 11. It can be found that the relative velocity increases along the streamwise direction and reaches the highest value at the regions near the outlet. The mean relative velocity in the whole channel increases with the increase of the flow rate. The semivolute spiral streamlines distribute smoothly and finally surround the impeller inlet. It is obvious that some vortexes appear in the vicinity of baffle tongue, which is because
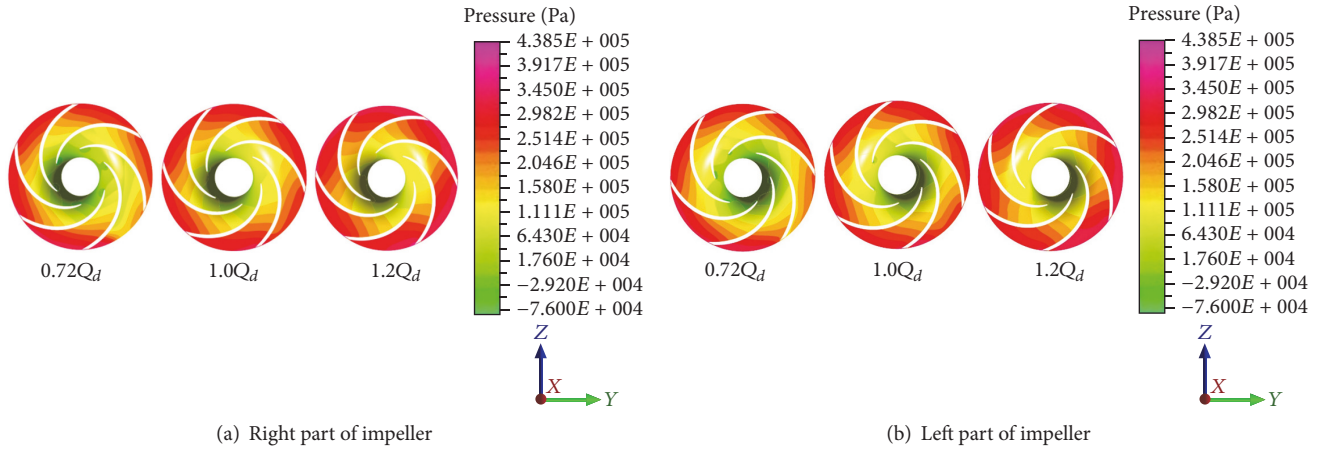
(a) Right part of impeller

(b) Left part of impeller

Figure 6: Static pressure distributions on impeller hub at different flow rates.
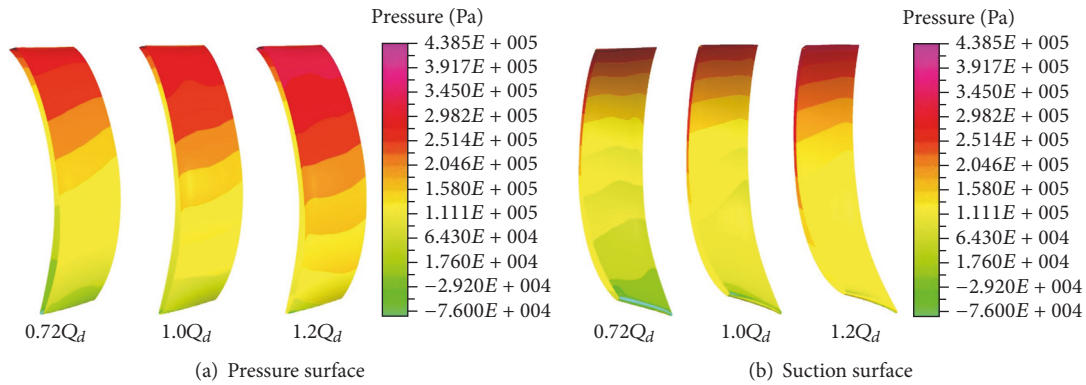

(a) Pressure surface

(b) Suction surface

Figure 7: Static pressure distribution on blade surfaces.

the liquid flow is blocked here. All the calculated results show that these vortexes gradually evolve, shedding from the vicinity of baffle tongue into the impeller, and bring velocity circulation here, which affects the hydraulic efficiency and the anticavitation performance of the impeller.

5.5. Distributions of Turbulence Kinetic Energy and Dissipation Rate in the Impeller. The distributions of turbulence kinetic energy k and turbulence dissipation rate ε in impeller from the inlet to the outlet are shown in Figures 12 and 13, respectively. In the figures, R_1 is the inlet radius of impeller, R_2 stands for the outlet radius, and R represents the radial distance between a point in the blade channels and the rotating center. It can be seen that the variation tendencies between k and ε are very similar. At different flow rates, k and ε increase at first and then decrease until reaching the minimum values in the middle of the flow channels and finally increase again. At the flow rate of $0.72Q_d$, there is a sharp increase in k and ε near the point of $(R-R_1)/(R_2-R_1) = 0.2$ due to the existence of axial vortexes here, which enlarge the energy dissipation. However, at the flow rates of $1.0Q_d$ and $1.2Q_d$, the changes of k and ε are relatively slow. On the whole, k and ε are lowest at design flow rate, which indicates that the efficiency is highest.

6. Analyses of Cavitation Characteristics

Normally, to avoid cavitation, the static pressure head at the pump inlet must be higher than the saturated vapor pressure by some margin, which is defined as the cavitation margin and is expressed as [18]

$$\text{NPSH}_a = \frac{p_{\text{in}} - p_v}{\rho g}, \tag{10}$$

where p_{in} and p_v represent the static pressure head at the pump inlet and the saturated vapor pressure, respectively. Figure 14 shows the predicted cavitation characteristic curve at design flow rate. If the point on the curve where the head drops by 3% is regarded as the critical cavitation point, NPSH_r of this pump at design flow rate is about 4.7 m.

6.1. Blade Loading Distribution in the Impeller. The blade loading is defined by the pressure difference between the pressure surface and the suction surface of one blade at the same radius location. The blade loading distribution of the middle streamlines on the blade surfaces under different cavitation margin conditions is shown in Figure 15, where L is the total length of the middle streamlines on the blade surfaces and l represents the distance from the blade inlet
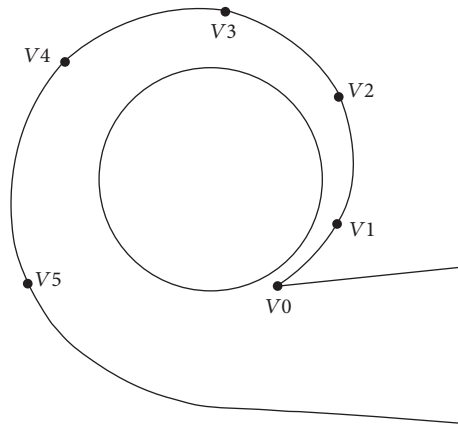
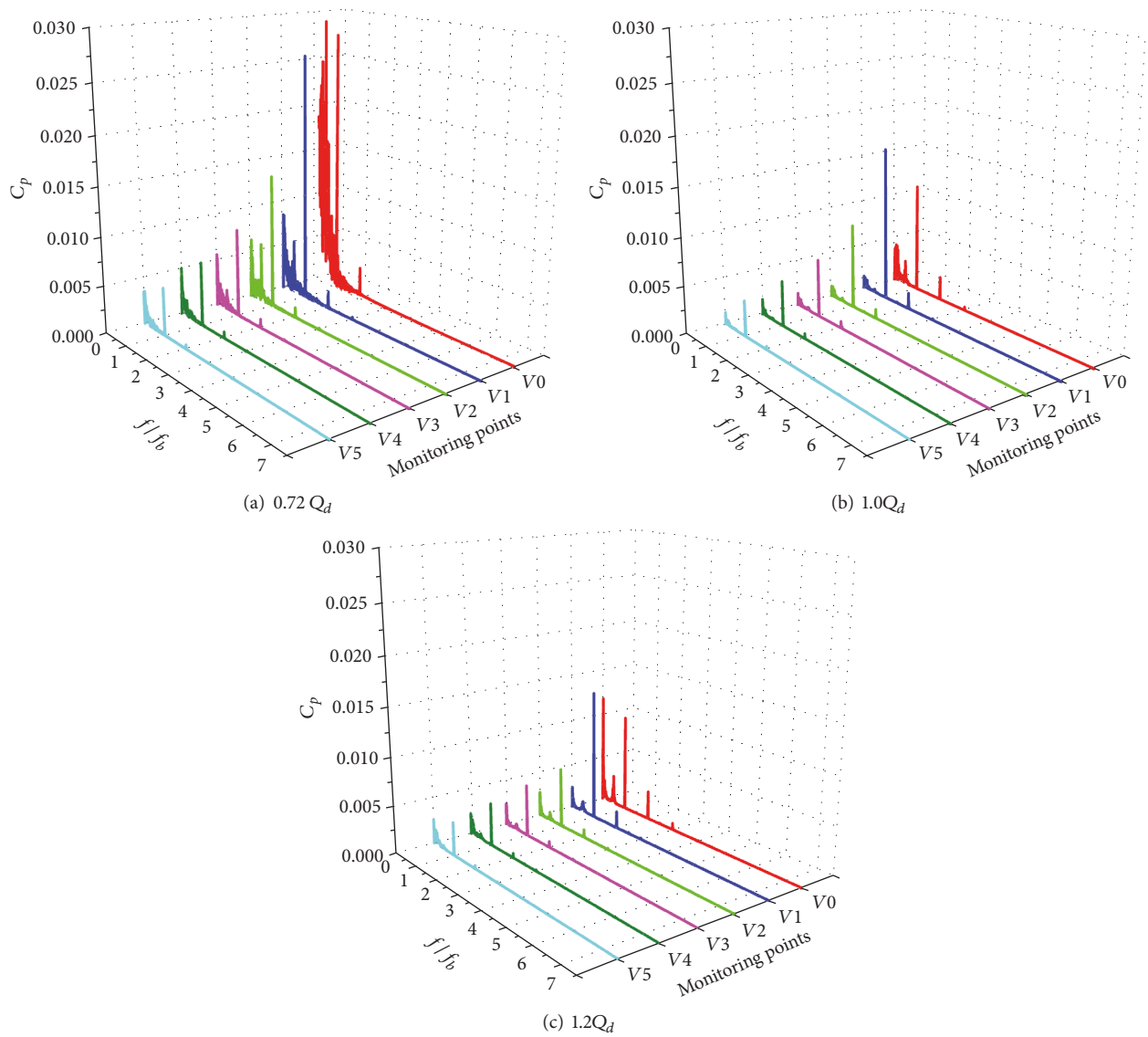FIGURE 8: Monitoring points in volute wall.

(a) 0.72 Q_d

(b) 1.0Q_d

(c) 1.2Q_d

FIGURE 9: Frequency domain of pressure fluctuations in volute casing at different flow rates.

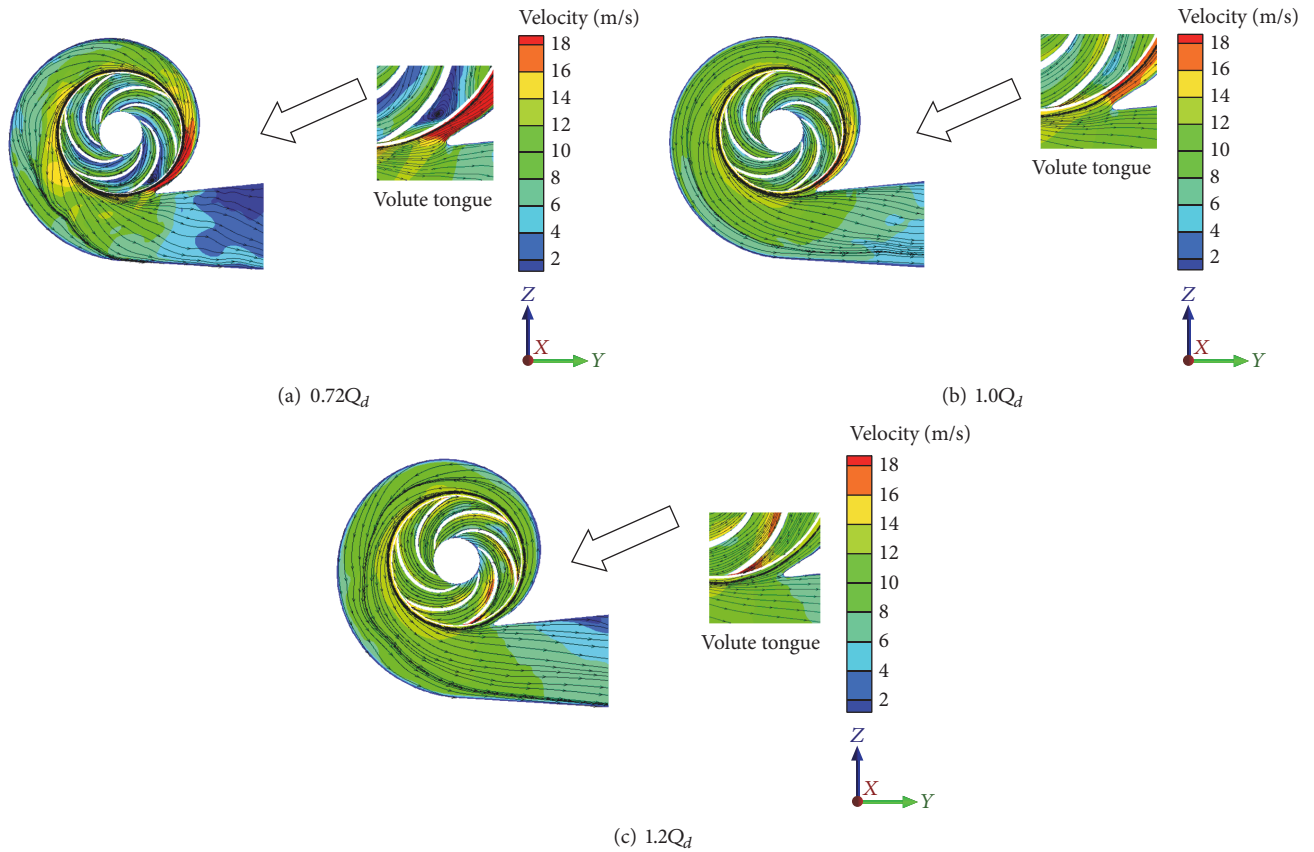(a) $0.72Q_d$

(b) $1.0Q_d$

(c) $1.2Q_d$

FIGURE 10: Relative velocity and streamline distributions in the impeller and volute casing.

edge to a point of the middle streamlines on the blade surfaces along the streamlines. It can be found that when $\mathrm{NPSH_a} = 11.4\,\mathrm{m}$ and $6.33\,\mathrm{m}$, the cavitation does not occur and the blade loading is not affected. Under the condition of $\mathrm{NPSH_a} = 4.27\,\mathrm{m}$, the pressure distribution of the middle streamline on the pressure surface does not change, but it obviously reduces on the suction surface, and thus it increases the blade loading. When $\mathrm{NPSH_a}$ drops to $3.94\,\mathrm{m}$, the cavitation is more serious, which makes the pressure in the middle streamlines on both the suction surface and the pressure surface of blade reduce a lot. In the positions from $l/L = 0$ to $l/L = 0.3$, the blade loading is almost 0 and even reaches negative values.

6.2. Vapor-Phase Volume Fraction Distribution in the Impeller. Figures 16 and 17 show the distribution of the vapor-phase volume fraction in the impeller under conditions of different $\mathrm{NPSH_a}$. It can be concluded that the vapor-phase volume fraction increases with the decrease in $\mathrm{NPSH_a}$, and the cavitation bubbles gradually spread from the impeller inlet to the outlet. And the bubbles mainly concentrate around the blade suction surfaces near the inlet, which is because of the low pressure appearing near the suction surfaces. When $\mathrm{NPSH_a} = 11.4\,\mathrm{m}$ and $6.33\,\mathrm{m}$, the vapor-phase volume fraction is almost 0 from the impeller inlet to the outlet, which indicates that the cavitation phenomenon does not appear and the pump head is not affected, which can be confirmed from the pump cavitation characteristic curves

shown in Figure 14. But when $\mathrm{NPSH_a} = 4.27\,\mathrm{m}$ and $3.94\,\mathrm{m}$, a large number of cavitation bubbles appear in the impeller; particularly when $\mathrm{NPSH_a} = 3.94\,\mathrm{m}$, the cavitation is more serious. The bubbles have blocked the blade channels, and the pump head drops by more than 20%. In addition, the distribution of vapor-phase volume fraction in the blade channels is nonaxisymmetric, which may be caused by the dynamic-static coupling between the tongue of the volute casing and the impeller.

6.3. Streamline Distribution in the Impeller. The streamlines in the impeller distribute smoothly under noncavitation condition as shown in Figure 18(a), while the streamline distribution in impeller channels is relatively disordered under cavitation condition as shown in Figure 18(b), which is caused by the secondary flows near the exit of the impeller. These vortices have great effects on the pump head, as is shown in Figure 14.

6.4. Power Distribution in the Impeller. The impeller is the key component of the pump for energy conversions. In addition, because the cavitation occurrence is closely related to the pressure, the power related to the pressure plays an important role in the impeller channels; the power P_{sec} on the cross section of the passage is defined as

$$P_{\mathrm{sec}} = \int_S p_t \mathbf{v} \cdot \mathbf{n}\, \mathrm{d}S, \tag{11}$$

(a) $0.72Q_d$
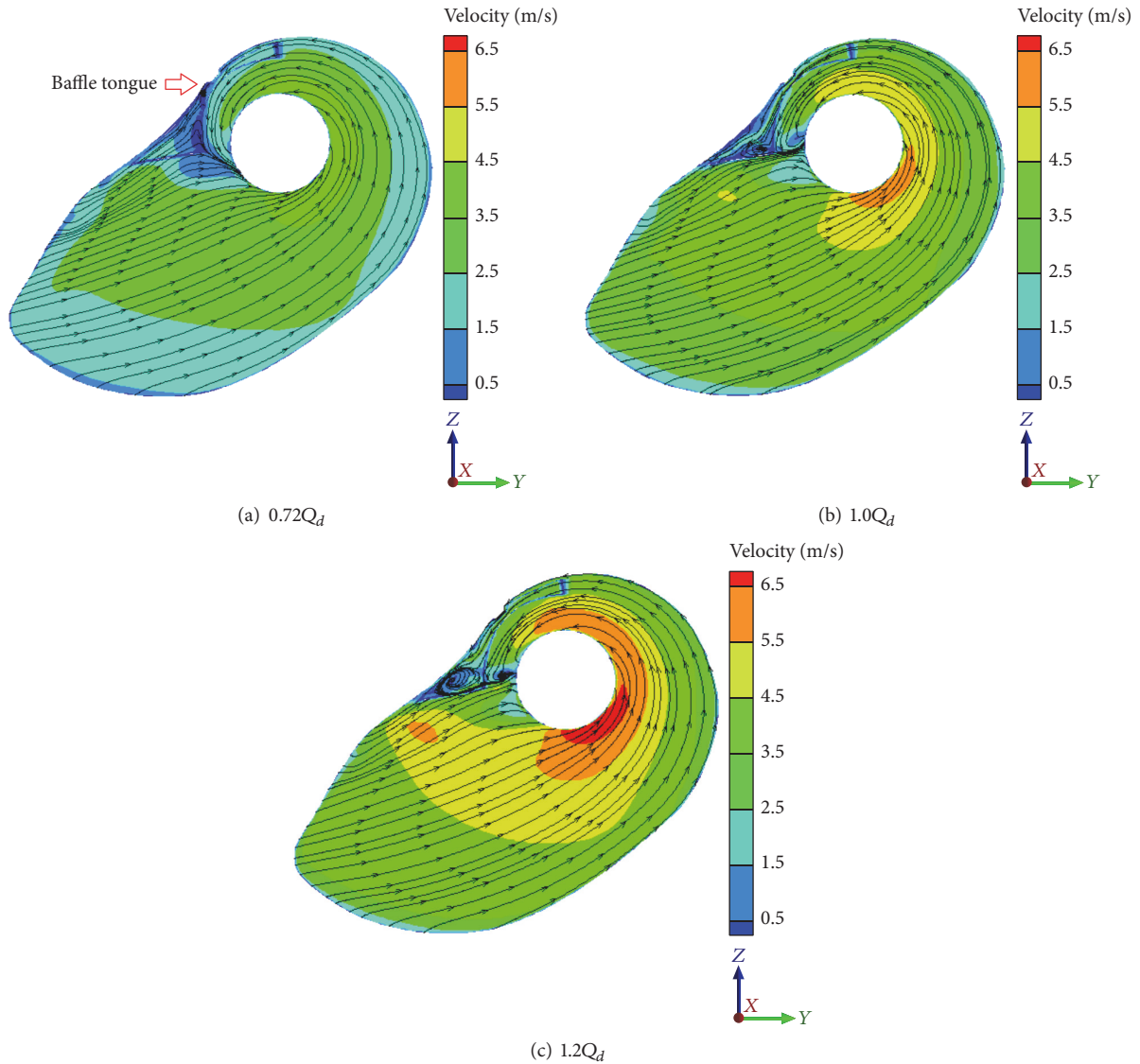
(b) $1.0Q_d$

(c) $1.2Q_d$

FIGURE 11: Relative velocity and streamline distributions in the suction chamber at different flow rates.

where p_t represents the total pressure of the fluid based on the absolute coordinate system, $\mathbf{v}$ represents the fluid absolute velocity, and $\mathbf{n}$ represents the unit vector normal to the cross section. And the integral term $p_t\mathbf{v} \cdot \mathbf{n}$ represents the power density on the cross section. 7 cross sections in each impeller channel are selected to investigate the power distribution, and these cross sections in impeller channels are located on the cylinders, the radii of which range from 60 mm to 174 mm as shown in Figure 19.

It can be seen from Figure 20 that the power in the impeller channels increases with the increase of the radius because the fluid obtains the work done by blades. In the blade leading regions, the power is very low and increases slowly for different NPSH$_a$ and its growth rate decreases as NPSH$_a$ decreases, which is related to the cavitation. In the blade middle regions, a sharp increase in the power occurs because a large proportion of energy conversion happens here, and

the energy conversion becomes worse for serious cavitation. In the blade trailing regions, the power increases slowly when NPSH$_a$ = 11.4 m and 6.33 m, and, in contrast, the secondary backflows cause drop in the power for NPSH$_a$ = 4.27 m and even sudden drop for NPSH$_a$ = 3.94 m, which can be confirmed by Figure 18. Overall, the power distribution in the left part of the impeller is the same as that in the right part of the impeller.

The power density distributions on the cylindrical cross sections in the impeller under noncavitation and cavitation conditions are shown in Figure 21. It can be seen that the power density on each cross section distributes nonuniformly, and the averaged power density on the cross sections in the impeller under noncavitation condition is larger than that under cavitation condition. In the same impeller channel, the averaged power density increases gradually from the inlet to the exit.
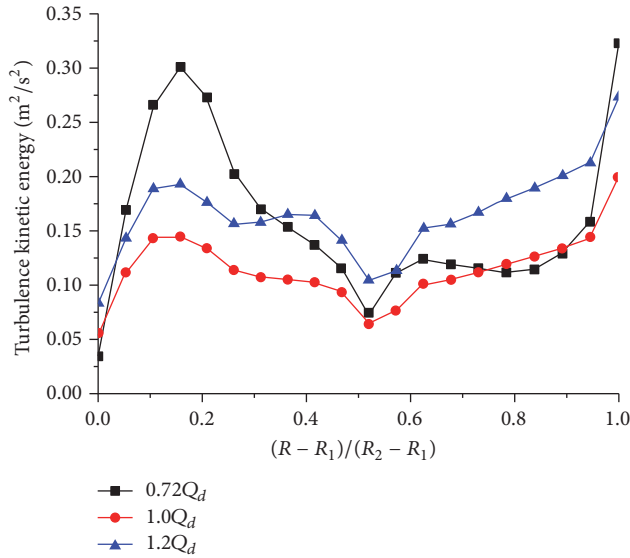
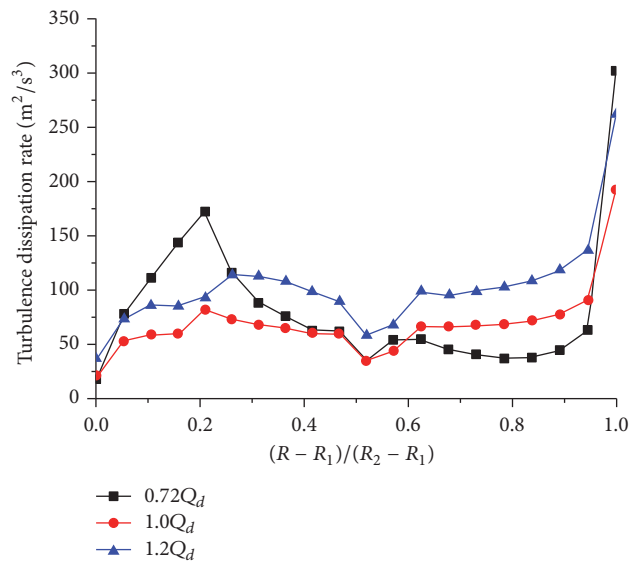FIGURE 12: The distribution of the turbulence kinetic energy k in the impeller at different flow rates.

FIGURE 13: The distribution of the turbulence dissipation rate ε in the impeller at different flow rates.

7. Conclusions

Based on the RNG k-ε turbulence model and the hexahedral structured grid, the unsteady flow inside a double-suction centrifugal pump was numerically investigated under different flow rate conditions. In addition, the blade loading and power distributions related to the cavitation at design flow rate were analyzed systematically. The results are listed and discussed as follows:

(1) The external and internal flow characteristics of the pump obtained by numerical simulation are in accord with the general law and agree well with the experimental results.
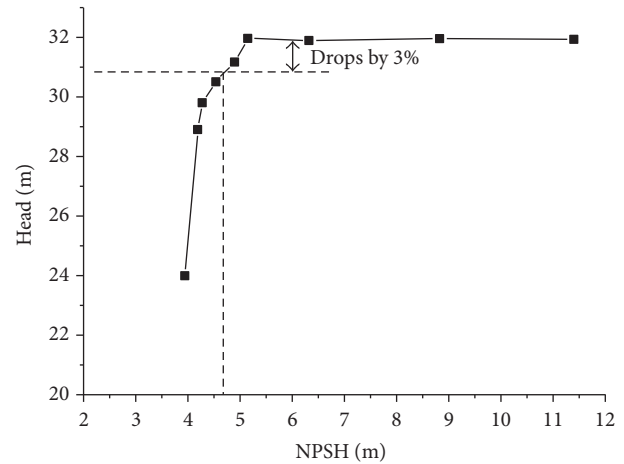

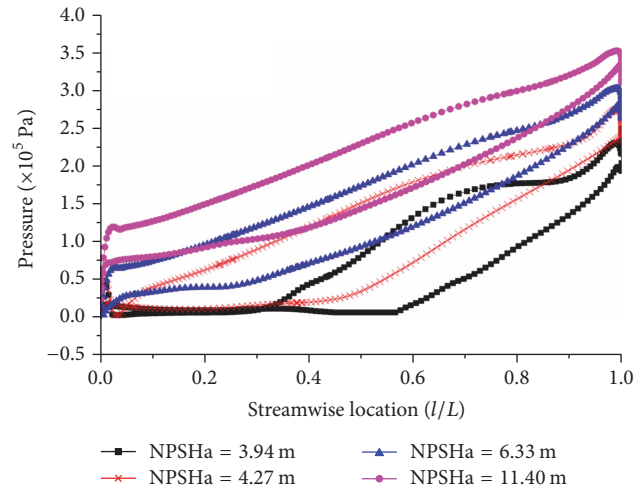FIGURE 14: Predicted cavitation characteristics curve.

FIGURE 15: Blade loading distribution on middle streamlines.

(2) The predicted variation tendencies of the turbulence kinetic energy k and the turbulence dissipation rate ε are very similar under different flow rate conditions, but k and ε at design flow rate are lower than those at other off-design flow rates.

(3) The blade passing frequency is the dominant frequency of the pressure fluctuations in the volute casing except the vicinity of the volute tongue for all operating cases, and the dominant one near the volute tongue is the blade passing frequency at the design point and 0~0.5 times the blade passing frequency at other off-design points.

(4) At the design flow rate, the cavitation causes the blade loading of the middle streamline to increase a bit during the initial stage, and serious cavitation causes the blade loading near the blade inlet to reduce to 0 and even negative values, which results in a sharp drop in the pump head.

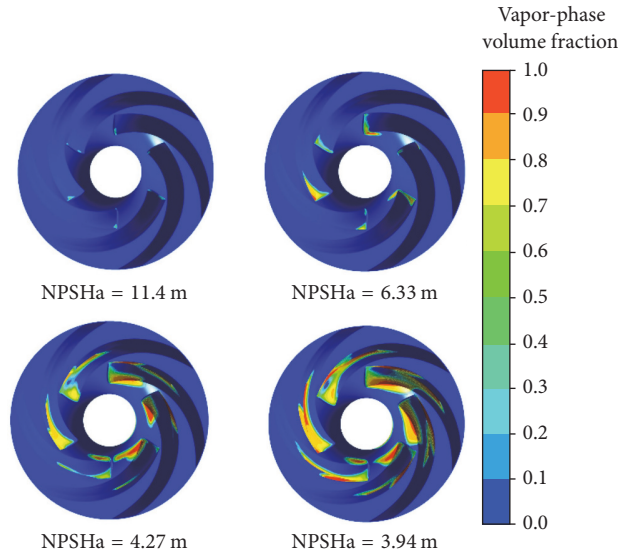(5) The power obtained from the impeller increases with the increase of radius in the whole impeller

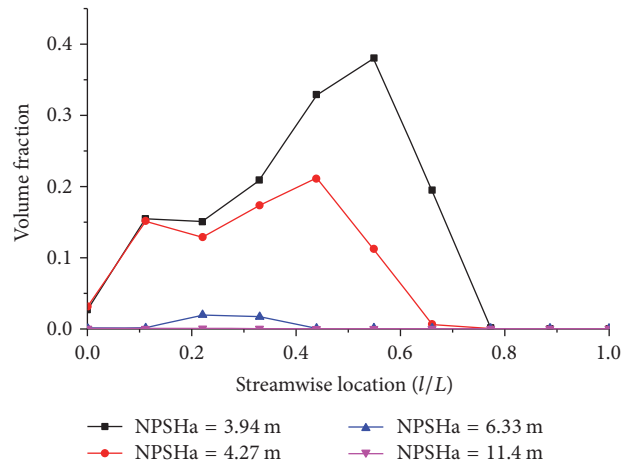FIGURE 16: Vapor-phase volume fraction distribution in the impeller.

FIGURE 17: The volume fraction curves of vapor phase in the impeller from inlet to outlet.
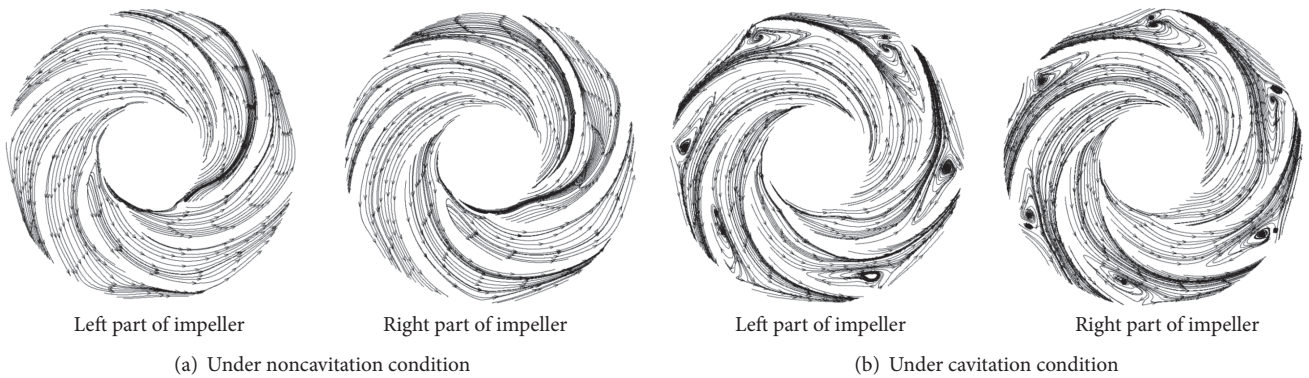

FIGURE 18: Streamline distribution in the impeller.
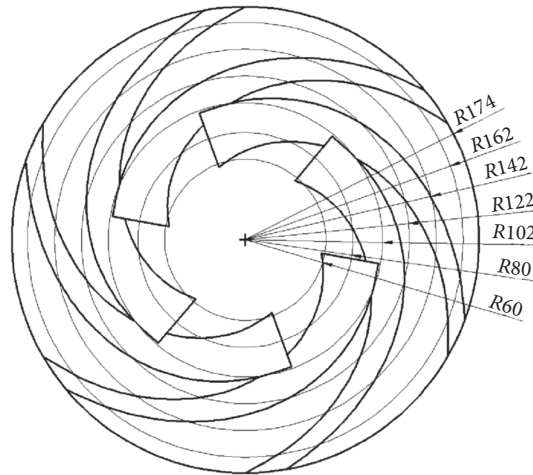
FIGURE 19: Sketch of impeller sections.

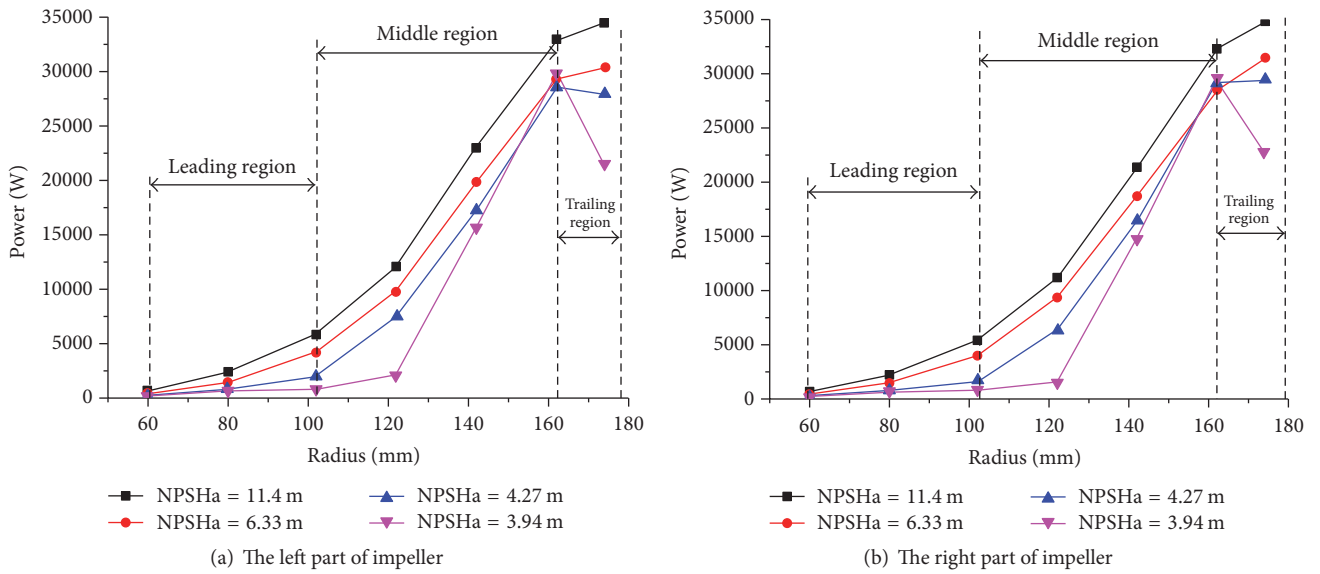(a) The left part of impeller

(b) The right part of impeller

FIGURE 20: Power curves of the impeller sections.

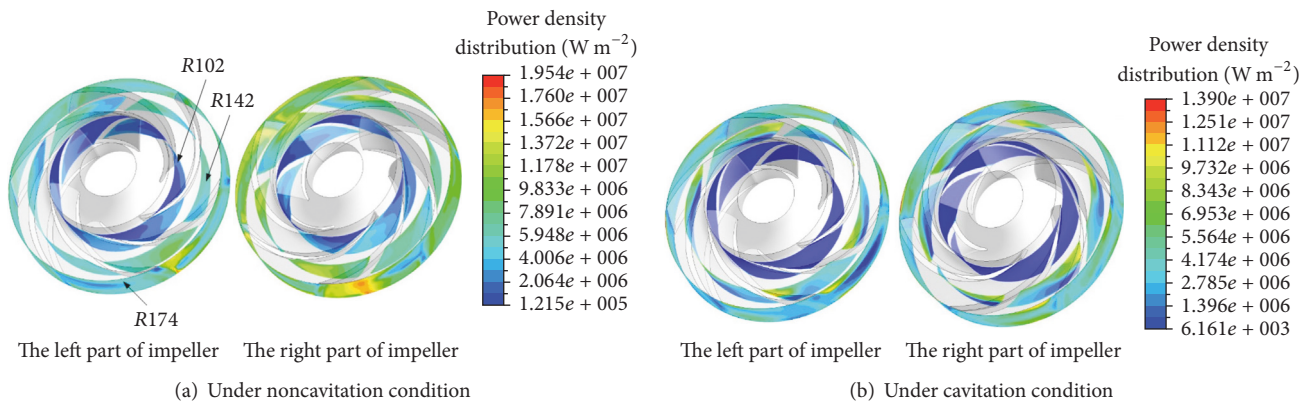(a) Under noncavitation condition

(b) Under cavitation condition

FIGURE 21: Power density contour of cross section ($R = 102, 142, 174$ mm).

channels, but the power in leading regions of the blades increases gradually a bit, and then it increases sharply in the middle regions. In the blade leading regions, the power increases slowly for noncavitation cases, while it decreases for cavitation cases; in particular, it suddenly drops for serious cavitation, which is caused by the secondary flows.

Nomenclature

D_{in}:   Pump inlet diameter
D_{out}:   Pump outlet diameter
D_1:   Inlet diameter of impeller
D_2:   Outlet diameter of impeller
D_3:   Cutwater diameter of volute casing
N: Blade number
n_s: Specific speed of the pump
H: Pump head
P: Pump shaft power
P_{sec}:   The power on the cross section of impeller
Q: Flow rate
η: Pump efficiency
η_m: Mechanical efficiency
η_v: Volumetric efficiency
η_h: Hydraulic efficiency
ρ: Fluid mass density
ρ_v: Mass density of vapor phase
p_v: Saturated vapor pressure of water
p: Transient pressure
C_p: Pressure coefficient
k: Turbulence kinetic energy
ε: Turbulence dissipation rate
$NPSH_a$:   Available net positive suction head
$NPSH_r$:   Required net positive suction head
m_{eva}:   Evaporation rate of water vapor
m_{con}:   Condensation rate of water vapor
C_{eva}:   Evaporation rate coefficient of water vapor
C_{con}:   Condensation rate coefficient of water vapor
T: The rotating period of the impeller
f_s: Sampling frequency
f_b: Blade passing frequency.

Conflicts of Interest

The authors declare that they have no conflicts of interest.

Acknowledgments

References

[1] R. Barrio, J. Parrondo, and E. Blanco, "Numerical analysis of the unsteady flow in the near-tongue region in a volute-type centrifugal pump for different operating points," *Computers & Fluids*, vol. 39, no. 5, pp. 859–870, 2010.

[2] N. Krause, K. Zähringer, and E. Pap, "Time-resolved particle imaging velocimetry for the investigation of rotating stall in a radial pump," *Experiments in Fluids*, vol. 39, no. 2, pp. 192–201, 2005.

[3] X. Luo, W. Wei, B. Ji, Z. Pan, W. Zhou, and H. Xu, "Comparison of cavitation prediction for a centrifugal pump with or without volute casing," *Journal of Mechanical Science and Technology*, vol. 27, no. 6, pp. 1643–1648, 2013.

[4] S. Shah, S. Jain, R. Patel, and V. Lakhera, "CFD for centrifugal pumps: a review of the state-of-the-art," *Procedia Engineering*, vol. 51, pp. 715–720, 2013.

[5] N. P. Jaiswal, "CFD analysis of centrifugal pump: a review," *Journal of Engineering Research and Applications*, vol. 4, pp. 175–178, 2014.

[6] T. Shigemitsu, J. Fukutomi, R. Nasada, and K. Kaji, "The effect of blade outlet angle on performance and internal flow condition of mini turbo-pump," *Journal of Thermal Science*, vol. 20, no. 1, pp. 32–38, 2011.

[7] S. Chakraborty, K. Choudhuri, P. Dutta, and B. Debbarma, "Performance prediction of Centrifugal Pumps with variations of blade number," *Journal of Scientific and Industrial Research*, vol. 72, no. 6, pp. 373–378, 2013.

[8] J. González, J. M. F. Oro, and K. M. Argüelles-Díaz, "Flow analysis for a double suction centrifugal machine in the pump and turbine operation modes," *International Journal for Numerical Methods in Fluids*, vol. 61, no. 2, pp. 220–236, 2009.

[9] X.-L. Tang, L.-Y. Bian, F.-J. Wang, X.-Q. Li, and M. Hao, "Numerical investigations on cavitating flows with thermodynamic effects in a diffuser-type centrifugal pump," *Journal of Mechanical Science and Technology*, vol. 27, no. 6, pp. 1655–1664, 2013.

[10] H. Liu, Y. Wang, D. Liu, S. Yuan, and J. Wang, "Assessment of a turbulence model for numerical predictions of sheet-cavitating flows in centrifugal pumps?" *Journal of Mechanical Science and Technology*, vol. 27, no. 9, pp. 2743–2750, 2013.

[11] Q. Thai and C. Lee, "The cavitation behavior with short length blades in centrifugal pump," *Journal of Mechanical Science and Technology*, vol. 24, no. 10, pp. 2007–2016, 2010.

[12] V. Yakhot and S. A. Orszag, "Renormalization group analysis of turbulence. I. Basic theory," *Journal of Scientific Computing*, vol. 1, no. 1, pp. 3–51, 1986.

[13] R. B. Medvitz, R. F. Kunz et al., "Performance analysis of cavitating flow in centrifugal pumps using multiphase CFD," *Journal of Fluids Engineering*, vol. 124, no. 2, pp. 377–383, 2002.

[14] A. K. Singhal, M. M. Athavale, H. Li, and Y. Jiang, "Mathematical basis and validation of the full cavitation model," *Journal of Fluids Engineering*, vol. 124, no. 3, pp. 617–624, 2002.

[15] T. Barth and D. Jespersen, "The design and application of upwind schemes on unstructured meshes," in *Proceedings of the 27th Aerospace Sciences Meeting*, Reno, NV, USA, 1989.

[16] G. Xingfan, *Modern Pumps Theory and Design*, Astronautics Press, Beijing, China, 2011.

[17] J. L. Parrondo-Gayo, J. González-Pérez, and J. Fernández-Francos, "The effect of the operating point on the pressure fluctuations at the blade passage frequency in the volute of a centrifugal pump," *Journal of Fluids Engineering*, vol. 124, no. 3, pp. 784–790, 2002.

[18] B. Ji, X. W. Luo, R. E. Arndt, X. Peng, and Y. Wu, "Large eddy simulation and theoretical investigations of the transient cavitating vortical flow structure around a NACA66 hydrofoil," *International Journal of Multiphase Flow*, vol. 68, pp. 121–134, 2015.

Advances in
Operations Research

Advances in
Decision Sciences

Journal of
Applied Mathematics

Algebra

Journal of
Probability and Statistics

The Scientific
World Journal

International Journal of
Differential Equations

International Journal of
Combinatorics

Advances in
Mathematical Physics

Submit your manuscripts at
https://www.hindawi.com

Hindawi

Journal of
Complex Analysis

Journal of
Mathematics

Mathematical Problems
in Engineering

Abstract and
Applied Analysis

Discrete Dynamics in
Nature and Society

International
Journal of
Mathematics and
Mathematical
Sciences

Journal of
Discrete Mathematics

Journal of
Function Spaces

International Journal of
Stochastic Analysis

Journal of
Optimization